scientific reports

Check for updates

OPEN

Narrow bandwidth, low-emittance positron beams from a laser-wakefield accelerator

M. J. V. Streeter[1], C. Colgan[2], J. Carderelli[3], Y. Ma[3], N. Cavanagh[1], E. E. Los[2], H. Ahmed[4], A. F. Antoine[3], T. Audet[1], M. D. Balcazar[3], L. Calvin[1], B. Kettle[2], S. P. D. Mangles[2], Z. Najmudin[2], P. P. Rajeev[4], D. R. Symes[4], A. G. R. Thomas[3] & G. Sarri[1]✉

The rapid progress that plasma wakefield accelerators are experiencing is now posing the question as to whether they could be included in the design of the next generation of high-energy electron-positron colliders. However, the typical structure of the accelerating wakefields presents challenging complications for positron acceleration. Despite seminal proof-of-principle experiments and theoretical proposals, experimental research in plasma-based acceleration of positrons is currently limited by the scarcity of positron beams suitable to seed a plasma accelerator. Here, we report on the first experimental demonstration of a laser-driven source of ultra-relativistic positrons with sufficient spectral and spatial quality to be injected in a plasma accelerator. Our results indicate, in agreement with numerical simulations, selection and transport of positron beamlets containing $N_{e+} \geq 10^5$ positrons in a 5% bandwidth around 600 MeV, with femtosecond-scale duration and micron-scale normalised emittance. Particle-in-cell simulations show that positron beams of this kind can be guided and accelerated in a laser-driven plasma accelerator, with favourable scalings to further increase overall charge and energy using PW-scale lasers. The results presented here demonstrate the possibility of performing experimental studies of positron acceleration in a laser-driven wakefield accelerator.

Plasma-based wakefield accelerators[1] have been gathering significant attention in recent years, mainly thanks to the ultra-high accelerating gradients (in the region of 10 s–100 GV/m) that they are able to sustain, providing a promising platform for the miniaturisation of particle accelerators. In addition, electron beams from a plasma accelerator naturally possess unique properties such as intrinsic femtosecond-scale duration, micron-scale source size, and sub-micron normalised emittances at the GeV level (see, e.g., Refs.[2,3]). Progress in laser and plasma technology can now also enable stable operation of these accelerators over long periods[4].

This rapid scientific and technological progress is now posing the realistic question as to whether plasma-based acceleration could be a viable complementary technology for the next generation of particle colliders, proposed to break the TeV barrier[5]. Several international consortia and proposed large-scale facilities are now actively addressing this question (e.g., Refs.[6,7]), which is also identified by several national and international roadmaps as a central area of research (see, e.g., Refs.[8–10]).

While plasma-based acceleration of electrons has achieved a relatively high level of maturity, plasma-based acceleration of positrons presents harder fundamental challenges. This is due to the inherent structure of the wakefield accelerating structures[11] as well as the stringent requirements on the temporal and spatial properties of the seed positron beam. For example, quasi-linear acceleration in a plasma with a density of $n_e = 10^{17}$ cm^{-3} (as proposed in baseline stuides, see e.g., Ref.[12]), would require longitudinal and transverse seed beam dimensions $\sigma_z, \sigma_x \lesssim 10$ µm. In order to achieve significant beam-loading conditions in the accelerator cavity, it is also necessary to inject significant amount of charge, typically in the region of 10s of pC[13]. For a future particle collider (e.g a Higgs factory) it will also be necessary to provide a higher charge ($\gtrsim 1$ nC) at a high energy (> 10 GeV)[14].

While several positron acceleration schemes have been theoretically proposed[15–21] and first proof-of-principle experiments have demonstrated potential in this direction[22–26], progress in this area has been hampered by the

[1]School of Mathematics and Physics, Queen's University Belfast, Belfast BT7 1NN, UK. [2]The John Adams Institute for Accelerator Science, Imperial College London, London SW7 2AZ, UK. [3]Center for Ultrafast Optical Science, University of Michigan, Ann Arbor, MI 48109-2099, USA. [4]Central Laser Facility, STFC Rutherford Appleton Laboratory, Didcot OX11 0QX, UK. ✉email: g.sarri@qub.ac.uk

scarcity of facilities capable of providing positron beams with these demanding characteristics. To date, only FACET-II[27] at SLAC could be in principle suited in the future for proof-of-principle experiments in this area.

In order to enable experimental studies of positron acceleration in a wakefield, it is thus necessary first to provide positron witness beams with high spatial and spectral quality at the GeV level. To achieve this goal, it would be desirable to avoid storage rings, so that the intrinsic femtosecond-scale duration of laser-driven positrons could be preserved. Laser-driven generation of ultra-relativistic positron beams is thus currently being actively studied, with several landmark results already reported, including maximum positron energies in the region of 100s of MeV[28–30], the generation of high-density and quasi-neutral electron-positron beams[31], and first experimental observation of pair-plasma dynamics[32]. However, to effectively enable plasma acceleration of positrons in the laboratory, it is necessary to produce beams that simultaneously have %-level energy spreads, femtosecond-scale duration, and micron-scale normalised emittance[5,7]. To date, properties of this kind have only been predicted numerically[29,33,34].

Here, we experimentally demonstrate that positron beams of this kind can be generated with a 150 TW laser. Crucially, we demonstrate that the obtained positron beams are of sufficient quality to be energy-selected, with our results showing the isolation of positron beamlets containing $\geq 10^5$ positrons in a 5% bandwidth at energies exceeding 500 MeV. These beams present femtosecond-scale duration and micron-scale normalised emittance, and are thus of sufficient spectral and spatial quality to act as a witness beam in a positron wakefield accelerator, as we demonstrate with proof-of-principle particle-in-cell simulations. Favourable scalings in the beam spectral and spatial characteristics already indicate that even higher quality can be achieved with laser systems of higher peak power[33,34]. These results represent a fundamental stepping-stone towards enabling widespread and systematic experimental studies of plasma-based positron acceleration.

Results

Experimental setup

The experiment was performed using the Gemini laser at the Central Laser Facility[35] (setup sketched in Fig. 1). The laser pulses contained a mean and rms variation of 7.9 ± 0.5 J in a FWHM pulse length of 48 ± 7 fs (peak power $P_0 = 156 \pm 9$ TW) and a central wavelength of 800 nm. The pulses were focused with an $f/40$ off-axis parabola into a gas jet from a 15 mm exit diameter nozzle, to generate high-energy electron beams via laser wakefield acceleration (LWFA) at a repetition rate of 1 shot every 20 seconds, as limited by the laser system. The gas was a mixture of 2% nitrogen and 98% helium and had an electron density of $n_e = (1.5 \pm 0.2) \times 10^{18}\,\mathrm{cm}^{-3}$, as measured via optical interferometry. The laser focal spot, measured in vacuum, was $(37 \pm 3) \times (52 \pm 4)$ µm in the transverse x and y directions respectively ($1/e^2$ radius), giving a peak intensity $I_0 = (3.1 \pm 0.3) \times 10^{18}\,\mathrm{Wcm}^{-2}$.

The residual laser exiting the LWFA was removed by reflection from a self-generated plasma mirror on the surface of a 125 µm polyimide tape which was replenished after every shot. The tape target was kept for all the experimental data shown here and was used to protect objects in the beam path (e.g. the converter described below) from laser damage and to prevent debris in the vacuum chamber. A movable lead converter target (placed at a distance $z_D = 50$ mm from the LWFA exit plane of the gas jet) was used to generate electron-positron beams through a two-step bremsstrahlung-induced Bethe-Heitler process[36]. The converter was a 45-degree wedge, such that translating it perpendicularly to the electron beam axis allowed the effective converter thickness to be varied continuously over the range $1 \geq L \geq 25$ mm.

A shielding lead wall with an on-axis 10 mm diameter aperture was placed to allow only particles emitted from the converter within a 12.6 mrad half-angle to propagate to the detectors. A permanent magnetic dipole (Dipole 1 in Fig. 1, with integrated strength of $B_x z = 0.3$ Tm) was placed behind the lead wall to sweep electrons and positrons onto the primary scintillator screens (LP1 and LE1, both Kodak LANEX) either side of the central axis, allowing observation of particles with kinetic energy $E \geq 200$ MeV. Due to experimental limitations, the two screens were placed at slightly different distances from the dipole and angles from the main axis: 134 cm and 41.1° for the positron side of the spectrometer (LP1 in Fig. 1) and 137 cm and 45.4° for the electron side of the spectrometer (LE1 in Fig. 1). A second scintillator screen (LE2) was placed 1 m behind the first in order to increase the measurement accuracy of the high energy electrons (more details in the "Methods" section). A second identical magnetic dipole (Dipole 2 in Fig. 1) with a 25 mm wide lead slit placed at its entrance was positioned in the dispersed positron beam, in a dog-leg configuration. The slit performed energy selection on the dispersed positron beam, which was then collimated onto an additional scintillator screen (LP2) by the magnet.

A 5.0 mm thick tungsten mask composed of horizontal slits with a period of 1100 µm (550 µm gaps) was placed into the beam axis 290 mm behind the rear face of the converter (see Fig. 1) to perform energy-resolved

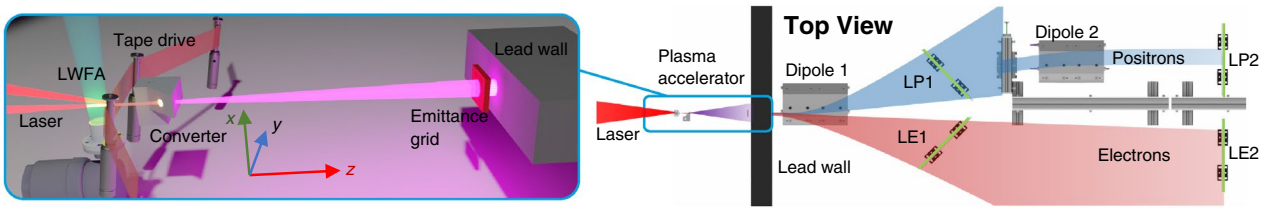

Figure 1. Illustration of the experimental setup. showing the electron plasma accelerator, the converter, the emittance mask, scintillators for electrons (LE1 and LE2) and positrons (LP1 and LP2). Electron (red) and positron (blue) trajectories are also shown to guide the eye.

emittance measurements on the generated positrons and the scattered electrons (details on the emittance retrieval in the "Methods" section and in the Supplemental material).

Experimental results

For sufficiently thick targets, positron generation in a solid converter mainly follows a two-step process, whereby a high energy photon generated via bremsstrahlung undergoes Bethe-Heitler pair production in the nuclear field[36]. This process results in a broadband distribution of the energy of the generated electron-positron pairs, irrespective of the spectrum of the primary electron beam. The LWFA was thus set up to generate high electron beam charge in a large energy spread, in order to maximise the yield of electron-positron pairs generated in the converter.

The electron spectra produced by the LWFA were first characterised with the tape drive in place but without the converter. Ten shots were taken with nominally identical conditions, with variations in the electron spectrum (30% relative rms variation in total charge) due to inherent variations in laser and plasma source parameters. The five shots with the highest total beam energy are shown in Fig. 2a. The angularly integrated electron spectra for each of these shots are plotted in Fig. 2b along with their average. When analysing the electron-positron beams, shots with the highest total charge (3–8 shots out of 10) were used for each converter length in order to maximise the accuracy of the emittance retrieval. Therefore, the average shown in Fig. 2b was taken as the expected LWFA spectrum for those shots. The average charge for electron energies above 200 MeV of the selected shots was $Q_b = 1.4 \pm 0.2$ nC, corresponding to a total beam energy of $W_b = 0.8 \pm 0.1$ J. The rejected shots had, instead, a slightly lower total charge of $Q_b = 0.9 \pm 0.3$ nC. The angular distribution of the energy integrated electron spectra was partially affected by the propagation through the tape target[37] and is closely approximated by the square of a Lorentzian function with a FWHM of $\theta_{\mathrm{FWHM}} = (3.8 \pm 0.4)$ mrad.

To demonstrate energy selection of laser-driven positron beams, a lead converter thickness of 5.0 mm (0.9 radiation lengths) was used and the recorded positron spectra after the second dipole magnet are shown in Fig. 3 for different transverse positions of the slit. For central energies of $E > 500$ MeV, more than 10^5 positrons per shot were transmitted within a FWHM bandwidth of $\Delta E/E \leq 5\%$, demonstrating the possibility of performing energy selection and capture of laser-driven positron beams of this kind. Similar results were obtained for different target thicknesses (not shown).

The energy-resolved emittance of the electrons and positrons exiting the converter target were characterised for different converter thicknesses by inserting the tungsten mask in front of the lead shielding wall (see Fig. 1). This insertion resulted in a modulated beam profile onto the scintillators, as shown in Fig. 4. The modulation had a lower spatial frequency at low energy, since particles with an energy $E \lesssim 300$ MeV exited the side of the dipole field and experienced defocusing as their longitudinal momentum (p_z) coupled with the transverse fringe field (B_y). In order to correct for the fringe field defocusing effect in the analysis, the measured signals were re-scaled in the non-dispersion direction such that the magnification of the grid pattern was kept constant for all energies. This results in an overestimation of the source size by $\sim 5\%$ for energies $E < 300$ MeV. In addition, the finite spectral resolution of the spectrometer caused blurring of the grid pattern where the magnification varied most strongly. As a result, the source size has a total systematic uncertainty of $\sim 30\%$ for $E < 350$ MeV. For $E > 350$ MeV, the blurring effect had a negligible effect on the measured source size.

The beam divergence $\sigma_\theta = \sqrt{\langle x'^2 \rangle}$ was found for each energy slice by fitting the envelope of the background subtracted signal and dividing by the source-to-screen distance. The non-zero source size (assumed to be Gaussian[33]) of the electron and positron beams resulted in a convolution of the detector resolution limited

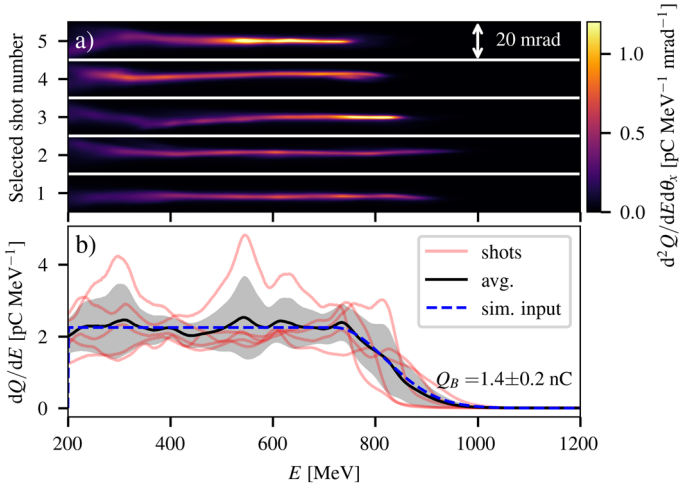

Figure 2. Primary electron beam characteristics. Typical (**a**) angularly resolved and (**b**) angularly integrated electron spectra of the LWFA electron beams (red). The average (black) and standard deviation (grey) of the integrated electron spectra are shown along with the approximation used as an input for the positron generation simulations (blue).

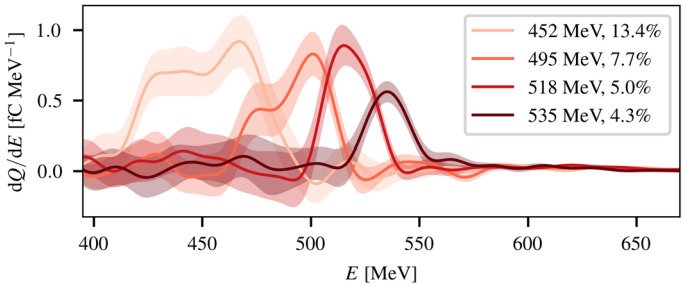

Figure 3. Narrow energy spread positron beams. Typical single-shot positron spectra measured after energy selection for different positions of the energy selection slit. Raw data has been background-subtracted and smoothed with a 10 MeV Gaussian filter, with the shaded region representing the local rms scatter of the data. The central energy and FWHM bandwidth of each spectrum is indicated in the figure legend.

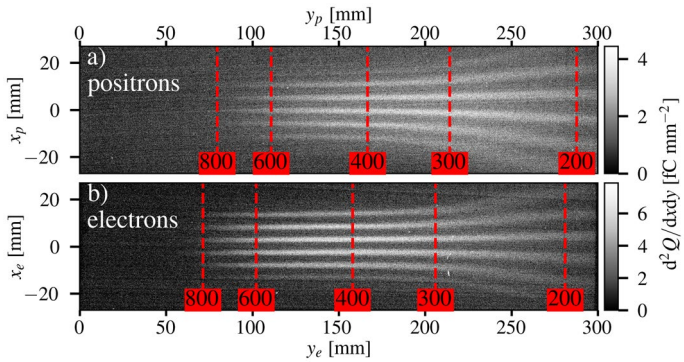

Figure 4. Raw images of energy-resolved beam profiles with the emittance mask. Example modulated (**a**) positron and (**b**) electron spatial charge density as a function of position on the screens (x_p, y_p, x_e, x_e) for a single shot with a converter thickness of 8.0 mm and the emittance mask in the beam-line. The positions corresponding to the given particle energies in MeV are shown as vertical red dashed lines. The slight difference between the electron and positron raw data is due to the slightly different position of the scintillator screens (discussed in the text).

grid pattern with a Gaussian distribution with an rms width of $\sigma_s = \sigma_x M$. The value σ_s was found by iterative deconvolution, and then divided by the source plane magnification, M, to yield the source size (rms) $\sigma_x = \sqrt{\langle x^2 \rangle}$.

The geometric emittance of a particle beam is defined as $\varepsilon = \sqrt{\langle x^2 \rangle \langle x'^2 \rangle - \langle xx' \rangle}$, where $\langle xx' \rangle$ is the angle-position correlation term. In the drift space between the LWFA and the converter, the primary electron beam develops a strong correlation term. However, the relatively large scattering angles in the converter dominate so that, at the exit of the converter, the positron beam is largely uncorrelated. Monte-Carlo simulations (discussed in the following) indicate that the small level of remaining correlation implies that the positron beam is equivalent to an uncorrelated beam originating from 100 to 200 µm inside the rear surface of the converter. Therefore, the correlation term was neglected and the geometric emittance was calculated as the product of the measured divergence and source size, i.e. $\varepsilon = \sigma_x \sigma_\theta$.

The electron and positron beam properties were measured as functions of energy for converter lengths $L = 1.0, 2.0, 4.0, 8.0$ mm (0.2, 0.4, 0.7 and 1.4 radiation lengths) and are plotted in Fig. 5. The number of observed electrons was seen to decrease with converter thickness (Fig. 5a), while the number of positrons was maximised for $L = 4.0$ mm. As the converter thicknesses are less than or on the order of the radiation length of the material, electrons scattered from the primary electron beam dominate the yield of the measured electron–positron beams. Converter thicknesses of 4–5 radiation lengths would be required to obtain close to 50% positrons[31,32], but at a cost of a lower yield and a higher emittance. The electron and positron source size (Fig. 5b) was observed to weakly decrease with energy, from 140±10 µm at 300 MeV down to 110±10 µm at 600 MeV, with fluctuations between 200 and 300 MeV due to the systematic uncertainties described before. The electron and positron rms divergence (Fig. 5c) was approximately constant at $\sigma_\theta = 5.3 \pm 0.3$ mrad, as it was limited by the aperture in the lead wall. Due to the fixed beam divergence, the measured emittance trends were largely determined by the variation in source size. The positron geometric emittance exhibited a gradual linear decrease as a function of energy with values of $\varepsilon = 640$ nm at $E = 200$ MeV and $\varepsilon = 480$ nm at $E = 600$ MeV for a 1.0 mm converter. As numerically predicted previously[29], the positron geometric emittance (Fig. 5d) was consistently lower than that of the scattered electrons. The results had an rms variation of $\approx 43\%$ in the spectrum and $\approx 20\%$ in emittance, due to the shot-to-shot variation in the primary electron beam induced by fluctuations in the laser performance.

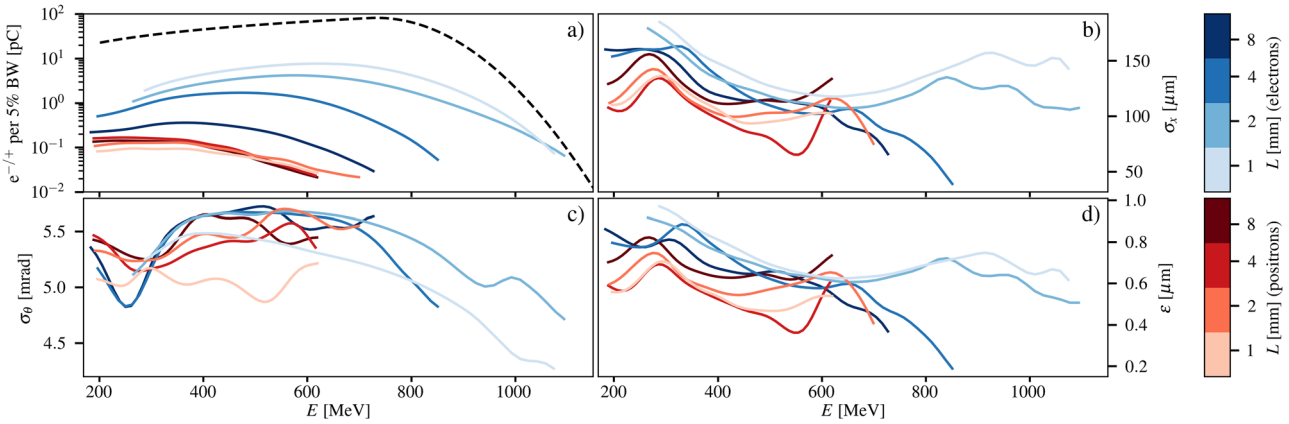

Figure 5. Positron properties as function of energy and converter thickness. Measured electron and positron beam properties as functions of particle energy for different converter thicknesses. The (**a**) spectra (charge per 5% bandwidth), (**b**) source size, (**c**) divergence and (**d**) geometric emittance are given for each converter length as shown by the color-bars at the side of the figure. For each converter thickness, only the shots resulting in the highest charge of the positron beams were used for the analysis; the lines shown are thus an average of 4, 6, 3 and 8 shots for converter lengths of 1.0, 2.0, 4.0 and 8.0 mm, respectively (rms variation of $\approx 43\%$ in the spectrum and $\approx 20\%$ in emittance, respectively). Each line results from a Gaussian weighting of each measurement point using a kernel width of $\sigma_E = 25$ MeV. The typical input electron spectrum (black-dashed) is shown in a) for comparison.

In order to ascertain the effect of the beam-line geometry on the measured positron beam characteristics, simulations were performed using the particle physics Monte-Carlo code FLUKA[38,39] (details in the Methods section and in the Supplemental material). Electrons were initialised from the LWFA electron spectrum approximation shown in Fig. 2b and the momenta and position of all electrons and positrons were recorded as they exited the rear surface of the converter. The divergence of the primary LWFA electron beam was modelled by applying randomised shifts (matching the measured LWFA divergence) to the position and propagation angles of each generated particle. The transverse particle positions were also modified according to the expected LWFA electron source size of 1 μm[40–42], although this contribution was observed to be negligible. The effect of the aperture in the beamline was simulated by removing all particles which had radial positions greater than 5 mm at the aperture plane.

For example, the results of the numerical simulation for a converter thickness of $L = 1.0$ mm show good agreement with the experimental data (blue and red lines in Fig. 6, respectively) with an rms average difference for all converter lengths of 15%, 3.5%, 2.8% and 0.5% for the spectrum, emittance, source size and divergence, respectively (see Supplemental material for results with other thicknesses).

Due to the higher initial divergence for lower energy particles, the aperture transmits a smaller fraction of lower energy positrons, modifying the detectable spectrum (Fig. 6a). The aperture also constrains the beam divergence to an approximately constant value of $\sigma_\theta \approx 5$ mrad (Fig. 6c). Including the finite divergence of the

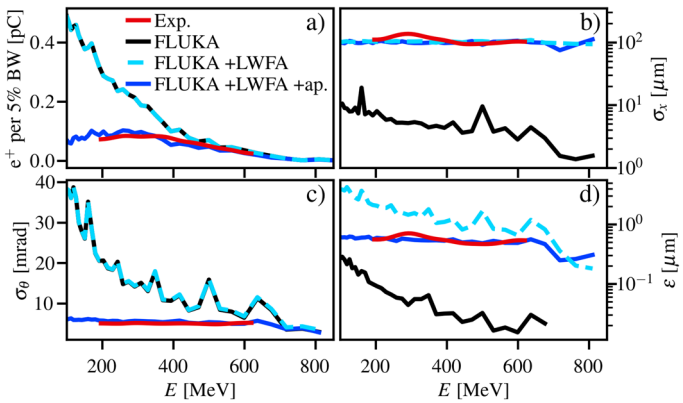

Figure 6. Comparison with numerical simulations. Positron beam (**a**) spectrum (charge per 5% bandwidth), (**b**) source size, (**c**) divergence and (**d**) geometric emittance plotted for a 1.0 mm thick lead converter. The experimental data (red) is plotted alongside FLUKA simulations for: zero drift distance for the primary electron beam (black); including the drift distance and the primary electron beam divergence and source size (cyan dashed); and including the 12.6 mrad shielding aperture (blue).

LWFA does not affect the positron spectrum or divergence but has a strong effect on the source size (Fig. 6b) and, subsequently, the emittance of the positron beam (Fig. 6d). In this case, the normalised emittance ($\varepsilon_n = \gamma\varepsilon$) increases with energy (unlike the FLUKA simulation only results), due to the combined effect of the drift space and the aperture.

A significant reduction in positron source size can be readily obtained by placing the converter closer to the exit of the LWFA, immediately after the tape drive or, alternatively, by using a beam transport system to minimise the electron beam size on the converter. A replenishing tape (such as the one used for this experiment) can be used to extract the post-plasma laser pulse and protect the converter from damage. As observed in our experiment, the laser-plasma interaction at the plasma mirror surface causes a small ($\sim$ mrad) increase in electron beam divergence[37], but this would be negligible compared to the inherent divergence of the pair production process.

Minimising the free-drift distance of the primary electron beam would dramatically improve the positron beam characteristics. For example, for the measured LWFA electron beam FWHM divergence of 3.8 mrad, a typical beam waist at the LWFA source of 1 μm, and a converter thickness of 1 mm, the positron source size at 600 MeV could be reduced to 2.7 μm. In this case the positron beam would have a divergence σ_θ =5.5 mrad, a geometric emittance ε =15 nm, and a normalised emittance $\bar{\varepsilon} = \gamma\beta_z\varepsilon = 18$ μm at 600 MeV. All positron beam parameters for different target thicknesses can then be readily obtained using known scaling laws (see, e.g., Refs.[33,34]). For a converter target placed right after the LWFA, our simulations indicate that different electron source size or divergence will have a small effect on the positron beam characteristics, which can anyway be taken into account by adding it in quadrature to the obtained values. For example, doubling the electron source size only increases the positron source size by approximately 10%. The simulations also show a spreading in the duration of the positron beam of 0.1 fs for positrons within a 5% bandwidth of 600 MeV implying that the positron beam duration will be similar to that of the primary electron beam (i.e., $\sigma_z \lesssim \lambda_p/2 = 14$ μm for $n_e = 1.5 \times 10^{18}$ cm^{-3}, corresponding to $\tau \lesssim 50$ fs).

Positron post-acceleration simulations

Simulations were performed using the particle-in-cell code FBPIC[43] to assess the suitability of the generated positron beams for post-acceleration in a plasma wakefield. As an example following a baseline study on plasma accelerators[12], the laser-wakefields were produced by the interaction of a Gaussian laser pulse with radius $r_L = 70$ μm, pulse length $\tau_L = 56$ fs and a normalised vector potential of $a_0 = 1.5$, with a pure helium plasma with an electron density of 2×10^{17} cm^{-3} and a length of 10 cm enclosed by two 0.5mm-long linear ramps.

The initial positron particle distribution was obtained from FLUKA simulations of the interaction of the LWFA electron beam with a 1 mm converter. A random shift of ±5 μm taken from a uniform probability distribution was added to the longitudinal position of each positron to approximate the effect of the primary electron bunch duration. This longitudinal spread is consistent with an upper limit of 14 μm estimated for the positron beams obtained in the experiment. The positron bunch was initialised at the peak of the positive accelerating field of the plasma wakefield. Further details of the simulation setup are given in the "Methods" section.

Figure 7 shows a summary of the main results of the simulation. For these laser and plasma conditions, a quasi-linear wakefield is generated behind the laser pulse (Fig. 7a) with a peak accelerating field of 13 GVm^{-1} and a period of 75 μm. After 96 mm of propagation in the plasma, 31% of the charge remains in a focused positron beam (Fig. 7b) which is accelerated to an average of 1.0 GeV with a relative rms energy spread of 20% (Fig. 7c,d). The beam is chirped, however, and so the energy spread could be reduced further using a plasma dechirper[44]. After an initial increase mainly due to a mismatch between the bunch emittance and the plasma focusing forces, the normalised emittance of the trapped positron beam remains approximately constant throughout the acceleration, at $\bar{\varepsilon} = 33.0 \pm 0.2$ μm.

These results can in principle be experimentally achieved by driving a laser wakefield accelerator directly behind the converter, as could be achieved with compact plasma mirror staging. This configuration can be directly implemented in existing and near-term laser facilities, enabling experimental studies of wakefield acceleration of positrons. Alternatively, a magnetic beam-line, as considered for example in EUPRAXIA[6], could be used to perform energy selection and controlled focusing to increase the experimental capabilities. As an example of this capability, we performed FBPIC simulations of wakefield acceleration of the energy-selected positron bunch (energy of 500 MeV with a 5% energy spread) in the same conditions as those discussed above (see Supplemental material for supporting figure). In this case, approximately 50% of the positron bunch is trapped and accelerated up to an energy of 1.2 ± 0.3 GeV with a normalised emittance of 57 μm.

Discussion and conclusions

With the minimisation of the drift length for the LWFA electrons, numerical simulations show that the obtained positron beam characteristics are now well suited to be captured and post-accelerated as a witness beam in a plasma wakefield accelerator. This result is also consistent with other studies reported in the literature. For example, Silva et al.[21] numerically demonstrated plasma acceleration for a positron bunch with a radius of $\sigma_x = 5$ μm and a normalised emittance of 10 μm using an electron beam driver, while Vieira et al.[17] numerically demonstrated effective wakefield acceleration of a $\sigma_x = 6$ μm positron beam in a Laguerre-Gaussian laser mode. Proof-of-principle experiments on wakefield acceleration of positrons reported in the literature[22–25], used witness positron beams with similar geometric emittance to our inferred beam properties, though at a higher energy (see Table 1), demonstrating the suitability of the positron source reported here to provide witness beams for wakefield acceleration studies, such as proposed for EuPRAXIA[6]. Most notably, the inherent short duration of the positron beam (inferred to be of the order of $\lesssim$ 50 fs) is naturally suited for injection in a positron-accelerating wakefield structure without the need for complex beam manipulation, as also confirmed by the proof-of-principle simulations reported in this article.

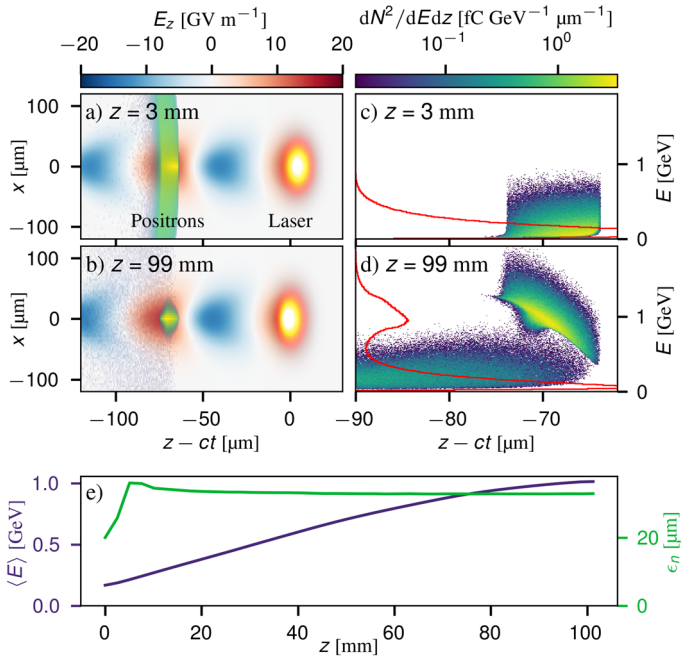

Figure 7. Simulated post-acceleration of a laser-generated positron beam. (**a**, **b**) show the longitudinal electric fields of the plasma wakefield generated by the laser pulse (yellow orb) and the trailing positron bunch (density in a logarithmic colour-scale) at the beginning of the plasma and after 96 mm of propagation. Panels (**c**, **d**) show the positron longitudinal phase space before and after acceleration, with the energy spectra indicated by the red lines. (**e**) shows the average energy and normalised emittance of the trapped bunch, defined as being comprised of particles which remain within ±50 μm of the central axis.

	Measured	Inferred	Muggli et al.[22]	Corde et al.[23]	Gessner et al.[24]
E (GeV)	0.6	0.6	28.5	20.3	20.3
σ_x (μm)	100	2.7	25	< 100	50
σ_z (μm)	–	$\lesssim 4^*$	730	30–50	35
ε (nm)	480	15	14 × 3	5 × 1	7
$\bar{\varepsilon}$ (μm)	560	18	390 × 80	200 × 50	300

Table 1. Summary of measured and inferred positron parameters, compared with sources used for previously reported proof-of-principle positron wakefield acceleration experiments. *Note that this value is the rms of a uniform distrubution with a width of 14 μm.

In conclusion, direct and comprehensive spatial and spectral characterisation of GeV-scale laser-driven positron beams is reported. Experimental results show that minimising the free propagation of the primary electron beam to the converter results in the production of GeV-scale positron beams with micron-scale source size and normalised emittance, using a 100 TW-class laser system. The beam is also shown to be of sufficient quality to undergo energy selection, with beamlets containing $\geq 10^5$ positrons in 5% bandwidths around 500 MeV being isolated, and of sufficient quality to be injected in a plasma wakefield accelerator. These results demonstrate the possibility of experimentally studying laser-wakefield acceleration of positrons. For instance, an experimental platform of this kind can be implemented in future laser facilities with dual beam capability[45] or even in beam-driven wakefield facilities with laser capability (e.g. FLASHForward[46] and SPARC_LAB[47]) to study beam-driven methods, without the need for an emittance damping storage ring.

In terms of future developments, increasing the stability and energy of the primary electron beam is expected to further improve the positron beam characteristics, with significant improvements in electron beam stability already having been reported with state-of-the-art laser systems[4]. Moreover, single-stage LWFA has been demonstrated beyond 5 GeV[48], which, in conjunction with a minimised drift distance for the LWFA electrons, is expected to readily provide, for instance, nm-scale geometric emittances and a normalised emittance of 10 μm at 3 GeV[33,34].

In addition, this positron generation mechanism is readily extendable to higher repetition rates, which will result in a dramatic enhancement in average positron flux. Operations of tape-drives, such as the ones used in this study, up to the kHz have already been demonstrated[49]. LWFA can also operate at kHz repetion-rates[50],

with fundamental limits due to plasma relaxation only in the MHz range[51]. Therefore, while our experiment was limited by the laser system to 1/20 Hz, it can be readily extended to the 10 Hz offered by modern PW lasers[45] and beyond, enabling a large increase in time-averaged positron yield.

It must be noted that, in order to study beam-loading effects by positrons in an LWFA, a higher positron beam charge ($\gtrsim 10$ pC) will be required. This could be enabled by increasing the energy of the primary electron beam while retaining its high charge[34].

As a final remark, we note that different mechanisms for the laser-driven generation of positron beams based on the Breit-Wheeler pair production process have also been numerically proposed (see, e.g., Refs.[52,53]). However, these mechanisms require next-generation multi-PW laser facilities and generally result in positron beams of different characteristics. Studies on direct irradiation of solid foils with the next generation of ultra-high intensity laser systems has also been numerically reported[54].

Methods

Two-screen electron spectrometer

Two scintillator screens were placed in the electron beam after the magnetic dipole, to detect electrons with kinetic energy in the range of $200 \geq \gamma m_e c^2 \geq 2500$ MeV and propagation angles relative to the laser propagation axis of $-15 \geq \theta_y \geq 15$ mrad. The 3D 3-vector field distribution of the dipole magnets was experimentally mapped and found in agreement with numerical simulations of the magnet setup using RADIA[55]. The screen dispersion functions were calculated by numerically solving the particle trajectories using the Boris-pusher and recording the particle position on each screen as a function of the initial particle 3-momentum. This was used to produce a look-up table which gave the particle energy as a function of its position on each screen and its initial propagation angle θ_y. The electron beam spectrum was determined by finding the coefficients of a third-order polynomial function $\theta_y(\gamma)$ that minimised the mean squared difference between the retrieved angularly integrated electron spectra from each screen. Using a third-order polynomial fit was found to be sufficient to match the observations from both spectrometer screens while ensuring a smooth solution that was robust to noise. Charge calibration of the electron spectrometers were performed by measuring electron spectra on an absolutely calibrated image plate placed in front of the LANEX screen and comparing to the images recorded on the CCD over the same shots. The image plate used was BAS-TR2040, with a sensitivity of 1 PSL per 350 electrons.

Source size, divergence, and emittance retrieval

The beam profile after the beam aperture was modelled as an azimuthally symmetric clipped Gaussian distribution, such that only particles with $x_{i,\mathrm{ap}}^2 + y_{i,\mathrm{ap}}^2 \leq R_{\mathrm{ap}}^2$ were transmitted, where $x_{i,\mathrm{ap}}$ and $y_{i,\mathrm{ap}}$ are the transverse spatial coordinates of the i^{th} particle at the aperture plane z_{ap}, with aperture radius R_{ap}. This profile was dispersed according to the individual particle energies onto the spectrometer screen. The particle distribution $S'_y(x)$ was measured at the detector plane z_{det} where x and y are transverse coordinates perpendicular and parallel to the dispersion plane of the spectrometer respectively. Due to the combination of energy spread and divergence, the profile $S'_y(x)$ is due to particles over a range of different energies where their initial propagation angle $\theta_{i,y}$ and energy E_i result in the particle intersecting the detector plane at the position y. With the assumption that the spectrum $N(E)$ is slowly varying, then each slice measurement $S'_y(x)$ represents the integral of the beam profile over y, i.e.,

$$\begin{aligned} S'_y(x) &= 2A_{y,0} \int_0^{\sqrt{R^2-x^2}} \exp\left[-\frac{x^2+y^2}{2\sigma_x^2}\right] \mathrm{dy} \\ S'_y(x) &= \sqrt{2\pi} A_{y,0} \sigma_x \mathrm{erf}\left(\sqrt{\frac{\mathrm{R}^2-\mathrm{x}^2}{2\sigma_{\mathrm{x}}^2}}\right) \exp\left[-\frac{\mathrm{x}^2}{2\sigma_{\mathrm{x}}^2}\right] \end{aligned} \tag{1}$$

where $A_{y,0}$ is the amplitude of the particle distribution, $R = R_{\mathrm{ap}} z_{\mathrm{det}}/z_{\mathrm{ap}}$ is the projected size of the aperture at the detector plane and $x \leq R$. The functional form of Eq. (1) was used to fit the amplitude of the modulated signal $S_y(x)$ when retrieving the apertured beam properties as described below.

Several steps were followed to extract the particle emittance from the spectrometer signals. Firstly, a variable threshold filter was used to remove hard-hits caused by stray photons hitting the CCD directly. Secondly, the defocusing of the effect of the magnetic dipole fringe fields was removed by re-scaling the measured signal in non-dispersion direction such that the spatial frequency of the grid pattern was made constant for all energies. Vertical slices were then taken through the resultant image, averaging over 4 mm in the dispersion direction to produce the signal modulation $S_y(x)$ as a function of x at a given y position. The scattered particles from the grid formed a smooth background on the detector which was removed by fitting a Gaussian to the values at the minima of the observed modulations. The envelope of the signal was similarly found by fitting the beam profile function (Eq. 1) to the signal maxima. The rms width of the fitted envelope was then divided by the source-to-screen distance to obtain the beam divergence σ_θ.

An ideal zero source size beam would produce a sharp step-function within the bounds of the scattering signal and the beam envelope, with the spatial period of the magnified grid size. Blurring of this pattern was observed due to contributions of the finite spatial resolution of the diagnostic (215 μm) and the source size σ_x of the beam, which was found by iterative minimisation of the mean squared error between the measured signal and the calculated signal for a given source size. The geometric emittance was calculated as the product of the measured divergence and source size, i.e. $\varepsilon = \sigma_x \sigma_\theta$.

In order to benchmark the retrieval process, synthetic data was created by numerically propagating results from a FLUKA simulation and removing particles that would hit the solid bars of the emittance measurement

grid. The dispersion of the magnet was added by shifting the particles transversely according to their energy using the same dispersion function as for the experimental spectrometer. To create the modulated signal $S_x(y)$ for a given energy band, the particles are selected according to their position on the spectrometer. Due to the significant beam divergence, there is some trajectory crossing such that some particles of different energies are selected, and some of the correct energy are omitted. The synthetic signals were analysed with the same procedure as for the experimental data and compared to the values directly calculated from the particle distributions. The retrieved beam properties closely agree with the directly computed values for the apertured beam, verifying the analysis procedure.

Monte-Carlo simulations
Simulations of the bremsstrahlung induced pair-production process were performed using the particle physics Monte-Carlo code FLUKA with the EM-cascade defaults. 10^6 primary electrons for each converter thickness were simulated and the resultant particle number was then scaled up by 8738 to match the higher charge of the experimental LWFA electron beam. A lead converter of variable thickness L was placed in the path of the electrons, and the momenta and position of all electrons, positrons and photons were recorded as they exited the rear surface of the converter. In order to simulate the effects of the finite divergence of the electron beam, each particle was assigned random angular shifts ($\Delta x_i'$ and $\Delta y_i'$) from the probability density function $f(x') = f_0[(x'/\theta_w)^2 + 1)]^{-2}$, which was seen to approximate the experimentally measured transverse profile of the primary electron beam with $\theta_w = 2.9 \pm 0.3$ mrad (f_0 is the normalisation constant). The particle transverse momenta and positions were then altered according to these shifts and using the experimental drift length between the LWFA exit and the converter rear face of 50 mm. The transverse particle positions were also modified according to the expected LWFA electron source size of 1 μm, although this contribution was negligible. Each particle was shifted 10 times from the value taken from the FLUKA simulation, with the shifted particle properties recorded each iteration to produce a final list with 10 times the number of particles as were produced by the FLUKA simulations. Particle distribution properties were then calculated at the longitudinal plane for which the correlation term $\langle xx' \rangle$ was minimised.

FBPIC simulations
The FBPIC Particle-In-Cell code[43] was used to run simulations of injection and acceleration of the output positrons from FLUKA Monte-Carlo simulations in a laser-driven wakefield. As FBPIC employs a cylindrical grid with azimuthal decomposition, two cylindrical modes were used to capture the physics of the wakefield formation and acceleration. The simulation was performed in the Lorentz boosted frame with a Lorentz factor of $\gamma = 10$. The wavelength of the laser was $\lambda_L = 1000$ nm, with a normalized vector potential of $a_0 = 1.5$. The background plasma profile consisted of a 0.5 mm linear up-ramp starting at the right-edge of the initial simulation window from vacuum to a plasma density of $n_{e0} = 2 \times 10^{17}$ cm^{-3} which was then constant for 100 mm. The plasma terminates with a 0.5 mm long down-ramp back to vacuum. The particles per cell set for each coordinate direction were 2 along $\hat{z}$, 2 along $\hat{r}$, and 6 along $\hat{\theta}$. The simulation box lengths were $z_{length} = \left(\frac{6c}{\omega_{p0}} + 2\lambda_{p0}\right) \approx 220.6\ \mu$m and $r_{length} = 2 \times r_{max} = 2 \times \frac{15c}{\omega_{p0}} \approx 2 \times 178.2\ \mu$m for $\hat{z}$ and $\hat{r}$ respectively, where $\omega_{p0} = \sqrt{\frac{e^2 n_{e0}}{\varepsilon_0 m_e}}$ is the plasma frequency of the peak initial density in the accelerator, and $\lambda_{p0} = \frac{2\pi c}{\omega_{p0}}$ is the plasma wavelength. The number of cells in each direction were for $\hat{z}$ $N_z = \lfloor \frac{z_{length}}{\Delta z} \rfloor = 1764$ where $\Delta z = \lambda_L/8$, and for $\hat{r}$ $N_r = \lfloor \frac{r_{max}}{\Delta r} \rfloor = 89$, where $\Delta r = 2 \times \lambda_L$. The time step size of the simulation was set to be $\Delta t = r_{max}/(2 \times \gamma \times N_r)/c \approx 0.334$ fs. The positrons simulated in Fig. 7 were imported into the FBPIC simulation from the output files given a random longitudinal spatial spread of 10 μm to match the inferred produced beam duration from this experimental campaign.

Data availability
All data generated or analysed during the this study are available from the corresponding author on reasonable request.

Received: 11 September 2023; Accepted: 4 March 2024
Published online: 12 March 2024

References
1. Esarey, E., Schroeder, C. B. & Leemans, W. P. Physics of laser-driven plasma-based electron accelerators. *Rev. Modern Phys.* **81**, 1229 (2009).
2. Weingartner, R. *et al.* Ultralow emittance electron beams from a laser-wakefield accelerator. *Phys. Rev. Special Topics Accelerators Beams* **15**, 111302 (2012).
3. Lundh, O. *et al.* Few femtosecond, few kiloampere electron bunch produced by a laser-plasma accelerator. *Nat. Phys.* **7**, 219 (2011).
4. Maier, A. R. *et al.* Decoding sources of energy variability in a laser-plasma accelerator. *Phys. Rev. X* **10**, 031039 (2020).
5. Adli, E. Plasma wakefield linear colliders-opportunities and challenges. *Philos. Trans. R. Soc. A Math. Phys. Eng. Sci.* **377**, 20180419 (2019).
6. Assmann, R. W. *et al.* EuPRAXIA conceptual design report. *Eur. Phys. J. Special Topics* **229**, 3675 (2020).
7. ALEGRO collaboration, Towards an Advanced Linear International Collider. arXiv https://doi.org/10.48550/arxiv.1901.10370 (2019)
8. Hidding, B., Hooker, S., Jamison, S., Muratori, B., Murphy, C., Najmudin, Z., Pattathil, R., Sarri, G., Streeter, M., Welsch, C., Wing, M., & Xia, G. Plasma Wakefield Accelerator Research 2019 - 2040: A community-driven UK roadmap compiled by the Plasma Wakefield Accelerator Steering Committee (PWASC), arxiv (2019).
9. N. G. Advanced Accelerator Development Strategy Report: DOE Advanced Accelerator Concepts Research Roadmap Workshop. https://doi.org/10.2172/1358081 (2016).

10. Adolphsen, C. *et al.* European Strategy for Particle Physics—Accelerator R &D Roadmap. https://doi.org/10.23731/CYRM-2022-001 (2022)
11. Lotov, K. V. Acceleration of positrons by electron beam-driven wakefields in a plasma. *Phys. Plasmas* **14**, 023101 (2007).
12. Schroeder, C. B., Esarey, E., Geddes, C. G. R., Benedetti, C. & Leemans, W. P. Physics considerations for laser-plasma linear colliders. *Phys. Rev. Special Topics Accelerators Beams* **13**, 101301 (2010).
13. Tzoufras, M. *et al.* Beam loading in the nonlinear regime of plasma-based acceleration. *Phys. Rev. Lett.* **101**, 145002 (2008).
14. Foster, B., D'Arcy, R. & Lindstrøm, C. A. A hybrid, asymmetric, linear Higgs factory based on plasma-wakefield and radio-frequency acceleration. *N. J. Phys.* **25**, 093037 (2023).
15. Kimura, W. D., Milchberg, H. M., Muggli, P., Li, X. & Mori, W. B. Hollow plasma channel for positron plasma wakefield acceleration. *Phys. Rev. Special Topics Accelerators Beams* **14**, 041301 (2011).
16. Yu, L. L. *et al.* Control of focusing fields for positron acceleration in nonlinear plasma wakes using multiple laser modes. *Phys. Plasmas* **21**, 120702 (2014).
17. Vieira, J. & Mendonça, J. T. Nonlinear laser driven donut wakefields for positron and electron acceleration. *Phys. Rev. Lett.* **112**, 215001 (2014).
18. Yi, L. *et al.* Positron acceleration in a hollow plasma channel up to TeV regime. *Sci. Rep.* **4**, 1 (2014).
19. Jain, N., Antonsen, T. M. & Palastro, J. P. Positron acceleration by plasma wakefields driven by a hollow electron beam. *Phys. Rev. Lett.* **115**, 195001 (2015).
20. Diederichs, S. *et al.* Positron transport and acceleration in beam-driven plasma wakefield accelerators using plasma columns. *Phys. Rev. Accelerators Beams* **22**, 081301 (2019).
21. Silva, T. *et al.* Stable positron acceleration in thin, warm, hollow plasma channels. *Phys. Rev. Lett.* **127**, 104801 (2021).
22. Muggli, P. *et al.* Halo formation and emittance growth of positron beams in plasmas. *Phys. Rev. Lett.* **101**, 055001 (2008).
23. Corde, S. *et al.* Multi-gigaelectronvolt acceleration of positrons in a self-loaded plasma wakefield. *Nature* **524**, 442 (2015).
24. Gessner, S. *et al.* Demonstration of a positron beam-driven hollow channel plasma wakefield accelerator. *Nat. Commun.* **7**, 1 (2016).
25. Doche, A. *et al.* Acceleration of a trailing positron bunch in a plasma wakefield accelerator. *Sci. Rep.* **7**, 1 (2017).
26. Lindstrøm, C. A. *et al.* Measurement of transverse wakefields induced by a misaligned positron bunch in a hollow channel plasma accelerator. *Phys. Rev. Lett.* **120**, 124802 (2018).
27. Yakimenko, V. *et al.* FACET-II facility for advanced accelerator experimental tests. *Phys. Rev. Accelerators Beams* **22**, 101301 (2019).
28. Sarri, G. *et al.* Table-top laser-based source of femtosecond, collimated, ultrarelativistic positron beams. *Phys. Rev. Lett.* **110**, 255002 (2013).
29. Alejo, A. *et al.* Non-invasive characterisation of a laser-driven positron beam. *Plasma Phys. Controlled Fusion* **62**, 055013. https://doi.org/10.1088/1361-6587/ab7e81 (2020).
30. Li, S. *et al.* A laser-plasma accelerator driven by two-color relativistic femtosecond laser pulses. *Sci. Adv.*https://doi.org/10.1126/sciadv.aav7940 *(2019).*
31. Sarri, G. *et al.* Generation of neutral and high-density electron-positron pair plasmas in the laboratory. *Nat. Commun.* **6**, 6747 (2015).
32. Warwick, J. *et al.* Experimental observation of a current-driven instability in a neutral electron–positron beam. *Phys. Rev. Lett.* **119**, 185002 (2017).
33. Alejo, A., Walczak, R. & Sarri, G. Laser-driven high-quality positron sources as possible injectors for plasma-based accelerators. *Sci. Rep.* **9**, 5279 (2019).
34. Sarri, G., Calvin, L. & Streeter, M. J. V. Plasma-based positron sources at EuPRAXIA. *Plasma Phys. Controlled Fusion* **64**, 044001 (2022).
35. Hooker, C. J. *et al.* The Astra Gemini project—A dual-beam petawatt Ti: Sapphire laser system. *J. Physique IV (Proceedings)* **133**, 673 (2006).
36. Sarri, G. *et al.* Laser-driven generation of collimated ultra-relativistic positron beams. *Plasma Phys. Controlled Fusion* **55**, 124017. https://doi.org/10.1088/0741-3335/55/12/124017 (2013).
37. Raj, G. *et al.* Probing ultrafast magnetic-field generation by current filamentation instability in femtosecond relativistic laser-matter interactions. *Phys. Rev. Res.* **2**, 023123 (2020).
38. Ferrari, A., Sala, P., Fasso, A. & Ranft, J. *FLUKA: A Multi-Particle Transport Code* Tech. Rep. (Stanford Linear Accelerator Center (SLAC), Menlo Park, CA, 2005).
39. Böhlen, T. *et al.* The FLUKA code: Developments and challenges for high energy and medical applications. *Nuclear Data Sheets* **120**, 211 (2014).
40. Kneip, S. *et al.* Bright spatially coherent synchrotron X-rays from a table-top source. *Nat. Phys.* **6**, 980 (2010).
41. Corde, S. *et al.* Mapping the X-ray emission region in a laser-plasma accelerator. *Phys. Rev. Lett.* **107**, 215004 (2011).
42. Wenz, J. *et al.* Quantitative X-ray phase-contrast microtomography from a compact laser-driven betatron source. *Nat. Commun.* **6**, 7568 (2015).
43. Lehe, R., Kirchen, M., Andriyash, I. A., Godfrey, B. B. & Vay, J.-L. A spectral, quasi-cylindrical and dispersion-free Particle-In-Cell algorithm. *Comput. Phys. Commun.* **203**, 66 (2016).
44. D'Arcy, R. *et al.* Tunable plasma-based energy dechirper. *Phys. Rev. Lett.* **122**, 034801 (2019).
45. Danson, C. N. *et al.* Petawatt and exawatt class lasers worldwide. *High Power Laser Sci. Eng.* **7**, 54 (2019).
46. Aschikhin, A. *et al.* The FLASHForward facility at DESY. *Nucl. Instrum. Methods Phys. Res. Section A Accelerators Spectrometers Detectors Associated Equipment* **806**, 175 (2016).
47. Ferrario, M. *et al.* SPARC-LAB present and future. *Nucl. Instrum. Methods Phys. Res. Sect. B Beam Interact. Mater. Atoms* **309**, 183 (2013).
48. Gonsalves, A. J. *et al.* Petawatt laser guiding and electron beam acceleration to 8 GeV in a laser-heated capillary discharge waveguide. *Phys. Rev. Lett.* **122**, 084801 (2019).
49. Haney, S. J., Berger, K. W., Kubiak, G. D., Rockett, P. D. & Hunter, J. Prototype high-speed tape target transport for a laser plasma soft-X-ray projection lithography source. *Appl. Opt.* **32**, 6934 (1993).
50. Gustas, D. *et al.* High-charge relativistic electron bunches from a khz laser-plasma accelerator. *Phys. Rev. Accel. Beams* **21**, 013401 (2018).
51. D'Arcy, R. *et al.* Recovery time of a plasma-wakefield accelerator. *Nature* **603**, 58 (2022).
52. Ribeyre, X., d'Humières, E., Jansen, O., Jequier, S. & Tikhonchuk, V. T. Electron-positron pairs beaming in the breit-wheeler process. *Plasma Phys. Controlled Fusion* **59**, 014024 (2016).
53. Li, Y.-F., Chen, Y.-Y., Wang, W.-M. & Hu, H.-S. Production of highly polarized positron beams via helicity transfer from polarized electrons in a strong laser field. *Phys. Rev. Lett.* **125**, 044802 (2020).
54. Song, H.-H., Wang, W.-M. & Li, Y.-T. Dense polarized positrons from laser-irradiated foil targets in the qed regime. *Phys. Rev. Lett.* **129**, 035001 (2022).
55. Elleaume, P., Chubar, O. & Chavanne, J. Computing 3D magnetic fields from insertion devices. *Proc. 1997 Particle Accelerator Conf. (Cat. No.97CH36167)* **3**, 3509 (1998).

Acknowledgements
The authors wish to acknowledge support from EPSRC (EP/V044397/1, EP/N027175/1, EP/V049577/1), STFC (ST/V001639/1), US NSF (Grant #2108075) and from the staff of the Central Laser Facility.

Author contributions
G.S. devised and proposed the experiment, which was numerically modelled and designed by T.A., L.C., J.C. and M.J.V.S.. The experiment was carried out by N.C., E.E.L., A.F.A., M.D.B., L.C., H.A., B.K., P.P.R., and D.R.S., under the overall coordination of M.J.V.S., C.C., and G.S. The data analysis was predominantly performed by M.J.V.S and the particle-in-cell simulations were carried out by J.C. and Y.M., under the supervision of A.G.R.T. The manuscript was written by G.S., M.J.V.S, and J.C. with input from S.P.D.M., Z.N., and A.G.R.T.

Competing interests
The authors declare no competing interests.

Additional information
Supplementary Information The online version contains supplementary material available at https://doi.org/10.1038/s41598-024-56281-1.

Correspondence and requests for materials should be addressed to G.S.

Reprints and permissions information is available at www.nature.com/reprints.

Publisher's note Springer Nature remains neutral with regard to jurisdictional claims in published maps and institutional affiliations.